

## Abstract

# Measurement of total hadronic differential cross sections in the LArIAT experiment

Elena Gramellini

2018

<sup>6</sup> Abstract goes here. Limit 750 words.

# **Measurement of total hadronic differential cross sections in the LArIAT experiment**

A Dissertation  
Presented to the Faculty of the Graduate School  
of  
Yale University  
in Candidacy for the Degree of  
Doctor of Philosophy

15 by  
16 Elena Gramellini

<sup>17</sup> Dissertation Director: Bonnie T. Fleming

<sup>18</sup> Date you'll receive your degree

<sup>19</sup>

Copyright © 2017 by Elena Gramellini

<sup>20</sup>

All rights reserved.

# <sup>21</sup> Contents

<sup>22</sup>	<b>Acknowledgements</b>	<b>v</b>
<sup>23</sup>	<b>0 LArIAT: Liquid Argon In A Testbeam</b>	<b>1</b>
<sup>24</sup>	0.1 The Particles' Path to LArIAT . . . . .	1
<sup>25</sup>	0.2 LArIAT Tertiary Beam Instrumentation . . . . .	4
<sup>26</sup>	0.2.1 Bending Magnets . . . . .	4
<sup>27</sup>	0.2.2 Multi-Wire Proportional Chambers . . . . .	6
<sup>28</sup>	0.2.3 Time-of-Flight System . . . . .	8
<sup>29</sup>	0.2.4 Punch-Through and Muon Range Stack Instruments . . . . .	9
<sup>30</sup>	0.2.5 LArIAT Cosmic Ray Paddle Detectors . . . . .	11
<sup>31</sup>	0.3 In the Cryostat . . . . .	12
<sup>32</sup>	0.3.1 Cryogenics and Argon Purity . . . . .	12
<sup>33</sup>	0.3.2 LArTPC: Charge Collection . . . . .	15
<sup>34</sup>	0.3.3 LArTPC: Light Collection System . . . . .	18
<sup>35</sup>	0.4 Trigger and DAQ . . . . .	20
<sup>36</sup>	0.5 Control Systems . . . . .	22
<sup>37</sup>	<b>1 Total Hadronic Cross Section Measurement Methodology</b>	<b>28</b>
<sup>38</sup>	1.1 How to Measure a Hadron Cross Section in LArIAT . . . . .	28
<sup>39</sup>	1.1.1 Event Selection . . . . .	29
<sup>40</sup>	1.1.2 Wire Chamber to TPC Match . . . . .	31

41	1.1.3	The Thin Slice Method . . . . .	33
42	1.1.4	Procedure testing with truth quantities . . . . .	36
43	<b>A</b>	<b>Measurement of LArIAT Electric Field</b>	<b>38</b>

# <sup>44</sup> Acknowledgements

<sup>45</sup> A lot of people are awesome, especially you, since you probably agreed to read this

<sup>46</sup> when it was a draft.

<sup>47</sup> **Chapter 0**

<sup>48</sup> **LArIAT: Liquid Argon In A**

<sup>49</sup> **Testbeam**

<sup>50</sup> In this chapter, we describe the LArIAT experimental setup. We start by illustrating  
<sup>51</sup> the journey of the charged particles in the Fermilab accelerator complex, from  
<sup>52</sup> the gaseous thermal hydrogen at the Fermilab ion source to the delivery of the LArIAT  
<sup>53</sup> tertiary beam at MC7. We then describe the LArIAT beamline detectors, the  
<sup>54</sup> LArTPC, the DAQ and the monitoring system.

<sup>55</sup> **0.1 The Particles' Path to LArIAT**

<sup>56</sup> LArIAT's particle history begins in the Fermilab accelerator complex with a beam of  
<sup>57</sup> protons. The process of proton acceleration develops in gradual stages (see picture  
<sup>58</sup> 1): gaseous hydrogen is ionized in order to form  $H^-$  ions; these ions are boosted to  
<sup>59</sup> 750 keV by a Cockcroft-Walton accelerator and injected into the linear accelerator  
<sup>60</sup> (Linac) that increases their energy up to 400 MeV; then,  $H^-$  ions pass through a  
<sup>61</sup> carbon foil and lose the two electrons; the resulting protons are then injected into a  
<sup>62</sup> rapid cycling synchrotron, called the Booster; at this stage, protons reach 8 GeV of  
<sup>63</sup> energy and are compacted into bunches; the next stage of acceleration is the Main

<sup>64</sup> Injector, a synchrotron which accelerates the bunches up to 120 GeV; in the Main  
<sup>65</sup> Injector, several bunches are merged into one and are ready for delivery.

<sup>66</sup> The Fermilab accelerator complex works in supercycles of 60 seconds in duration.

<sup>67</sup> A 120 GeV primary proton beam with variable intensity is extracted in four-second  
<sup>68</sup> “spills” and sent to the Meson Center beam line.

<sup>69</sup> LArIAT’s home at Fermilab is the Fermilab Test Beam Facility (FTBF), where  
<sup>70</sup> the experiment characterizes a beam of charged particles in the Meson Center beam  
<sup>71</sup> line. At FTBF, the primary beam is focused onto a tungsten target to create LAr-  
<sup>72</sup> IAT’s secondary beam. The secondary beamline is set such that the composition of  
<sup>73</sup> the secondary particle beam is mainly positive pions. The momentum peak of the  
<sup>74</sup> secondary beam was fixed at 64 GeV/c for the LArIAT data considered in this work,  
<sup>75</sup> although the beam is tunable in momentum between 8-80 GeV/c; this configuration  
<sup>76</sup> of the secondary beamline assured a stable beam delivery at the LArIAT experimental  
<sup>77</sup> hall.

<sup>78</sup> The secondary beam impinges then on a copper target within a steel collimator  
<sup>79</sup> inside the LArIAT experimental hall (MC7) to create the LArIAT tertiary beam,  
<sup>80</sup> (shown in Fig. 2). The steel collimator selects particles produced with a 13° pro-  
<sup>81</sup> duction angle. The particles are then bent by roughly 10° through a pair of dipole  
<sup>82</sup> magnets. By configuring the field intensity of the magnets we allow the particles of  
<sup>83</sup> LArIAT’s tertiary beam to span a momentum range from 0.2 to 1.4 GeV/c. The  
<sup>84</sup> polarity of the magnet is also configurable and determines the sign of the beamline  
<sup>85</sup> particles which are focused on the LArTPC. If the magnet polarity is positive the  
<sup>86</sup> tertiary beam composition is mostly pions and protons with a small fraction of elec-  
<sup>87</sup> trons, muons, and kaons. It is the job of the LArIAT beamline equipment to select the  
<sup>88</sup> particles polarity, to perform particle identification in the beamline and to measure  
<sup>89</sup> the momentum of the tertiary beam particles before they get to the LArTPC. The  
<sup>90</sup> LArIAT detectors are described in the following paragraphs.

## Fermilab Accelerator Complex

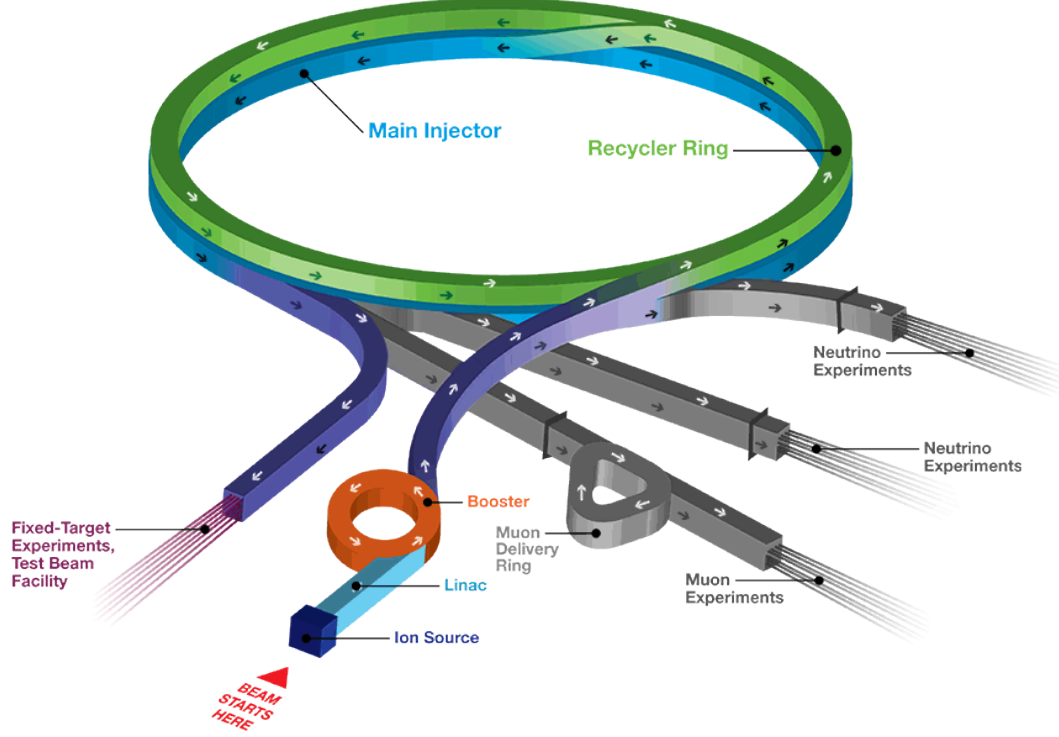


Figure 1: Layout of Fermilab Accelerator complex.

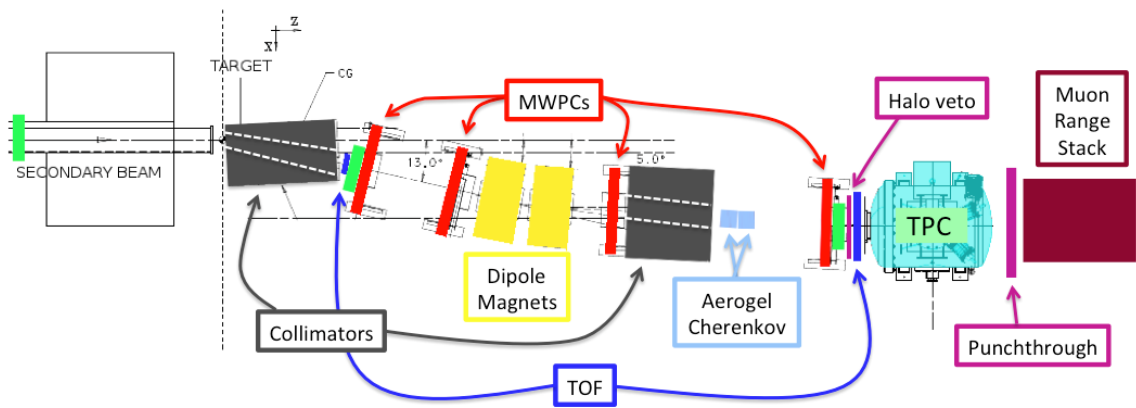


Figure 2: Bird's eye view of the LArIAT tertiary beamline. In grey: upstream and downstream collimators; in yellow: bending magnets; in red: multi wire proportional chambers; in blue: time of flight; in green: liquid argon TPC volume; in maroon: muon range stack.

## **91    0.2   LArIAT Tertiary Beam Instrumentation**

**92**   The instrumentation of LArIAT tertiary beam and the TPC components have changed  
**93**   several times during the three years of LArIAT data taking. The following paragraphs  
**94**   describe the components operational during “Run II”, the data taking period relevant  
**95**   to the hadron cross section measurements considered in this thesis.

**96**       The key components of the tertiary beamline instrumentation for the hadron cross  
**97**   section analyses are the two bending magnets, a set of four wire chambers (WCs)  
**98**   and two time-of-flight scintillating paddles (TOF) and, of course, the LArTPC. The  
**99**   magnets determine the polarity of the particles in the tertiary beam; the combination  
**100**   of magnets and wire chambers determines the particles’ momenta, which is used to  
**101**   determine the particle species in conjunction with the TOF. A muon range stack  
**102**   downstream from the TPC and two sets of cosmic paddles configured as a telescope  
**103**   surrounding the TPC are also used for calibration purposes. A couple of Aerogel  
**104**   Cherenkov counters, which we will not describe here as they are not used in the  
**105**   hadron cross section measurements, completes the beamline instrumentation.

### **106    0.2.1   Bending Magnets**

**107**   LArIAT uses a pair of identical Fermilab type “NDB” electromagnets, recycled from  
**108**   the Tevatron’s anti-proton ring, in a similar configuration used for the MINERvA  
**109**   T-977 test beam calibration [8]. The magnets are a fundamental piece of the LArIAT  
**110**   beamline equipment, as they are used for the selection of the particle polarity and  
**111**   for the momentum measurement before the LArTPC. The sign of the current in the  
**112**   magnets allows us to select either positively or negatively charged particles; the value  
**113**   of the magnetic field is used in the momentum determination and in the subsequent  
**114**   particle identification.

**115**       We describe here the characteristics and response of one magnet, as the second one

116 has a similar response, given its identical shape and history. Each magnet is a box with  
 117 a rectangular aperture gap in the center to allow for the particle passage. The magnet  
 118 aperture measures 14.22 cm in height, 31.75 cm in width, and 46.67 cm in length.  
 119 Since the wire chambers aperture ( $\sim 12.8$  cm $^2$ ) is smaller than the magnet aperture,  
 120 only the central part of the magnet gap is utilized. The field is extremely uniform  
 121 over this limited aperture and was measured with two hall probes, both calibrated  
 122 with nuclear magnetic resonance probes. The probes measured the excitation curve  
 123 shown in Figure 3.

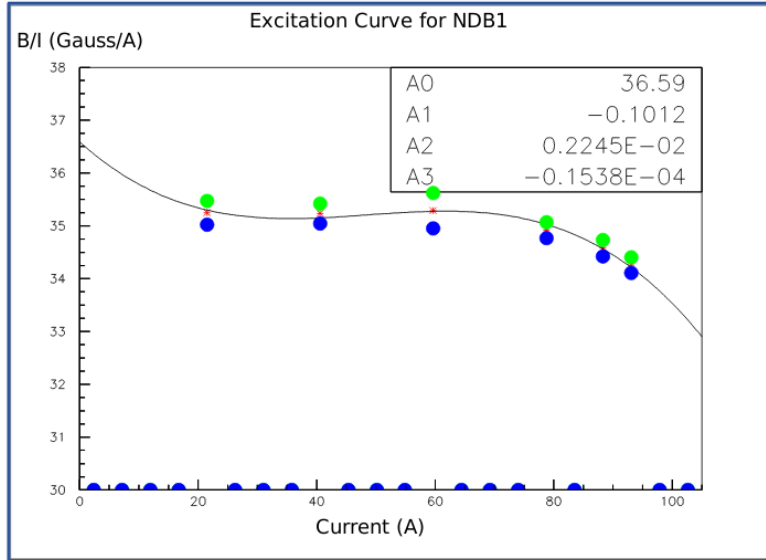


Figure 3: Magnetic field over current as a function of the current, for one NDB magnet (excitation curve). The data was collected using two hall probes (blue and green). We fit the readings with a cubic function (black) to average of measurements (red) given in the legend [7].

124 The current through the magnets at a given time is identical in both magnets.  
 125 For the Run II data taking period, the current settings explored were 60A ( $B \sim 0.21$   
 126 T) and 100A ( $B \sim 0.35$  T) in both polarities. Albeit advantageous to enrich the  
 127 tertiary beam composition with high mass particles such as kaons, we never pushed  
 128 the magnets current over 100 A, not to incur in overheating. During operation, we  
 129 operated an air and water cooling system on the magnets and we remotely monitored  
 130 the magnet temperatures.

<sub>131</sub> **0.2.2 Multi-Wire Proportional Chambers**

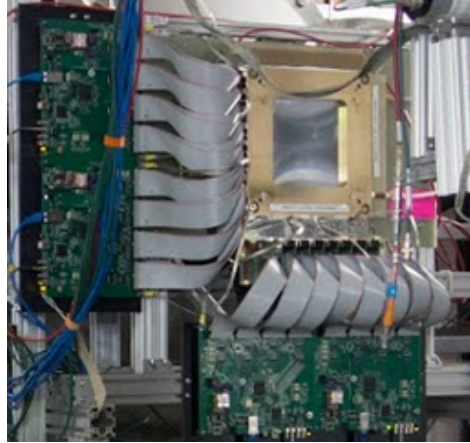


Figure 4: One of the four Multi Wire Proportional Chambers (WC) used in the LArIAT tertiary beamline and related read-out electronics.

<sub>132</sub> LArIAT uses four multi-wire proportional chambers, or wire chambers (WC) for  
<sub>133</sub> short, two upstream and two downstream from the bending magnets. The geometry  
<sub>134</sub> of one chamber is shown in Figure 4: the WC effective aperture is a square of 12.8 cm  
<sub>135</sub> perpendicular to the beam direction. Inside the chamber, the 128 horizontal and 128  
<sub>136</sub> vertical wires strung at a distance of 1 mm from each other in a mixture of 85% Argon  
<sub>137</sub> and 15% isobutane gas. The WC operating voltage is between 2400 V and 2500 V.  
<sub>138</sub> The LArIAT wire chambers are an upgraded version of the Fenker Chambers [11],  
<sub>139</sub> where an extra grounding improves the signal to noise ratio of the electronic readout.

<sub>140</sub> Two ASDQ chips [15] mounted on a mother board plugged into the chamber serve  
<sub>141</sub> as front end amplifier/discriminator. The chips are connected to a multi-hit TDC [14]  
<sub>142</sub> which provides a fast OR output used as first level trigger. The TDC time resolution  
<sub>143</sub> is 1.18 ns/bin and can accept 2 edges per 9 ns. The maximum event rate acceptable  
<sub>144</sub> by the chamber system is 1 MHz: this rate is not a limiting factor considering that  
<sub>145</sub> the rate of the tertiary particle beam at the first wire chamber is estimated to be less  
<sub>146</sub> than 15 kHz. A full spill of data occurring once per supercycle is stored on the TDC  
<sub>147</sub> board memory at once and read out by a specially designed controller. We use LVDS  
<sub>148</sub> cables to carry both power and data between the controller and the TDCs and from

<sub>149</sub> the controller to the rest of the DAQ.

<sub>150</sub> **Multi-Wire Proportional Chambers functionality**

<sub>151</sub> We use the wire chamber system together with the bending magnets to measure the  
<sub>152</sub> particle's momentum.

<sub>153</sub> In the simplest scenario, only one hit on each and every of the four wire chambers  
<sub>154</sub> is recorded during a single readout of the detector systems. Thus, we use the hit  
<sub>155</sub> positions in the two wire chambers upstream of the magnets to form a trajectory  
<sub>156</sub> before the bend, and the hit positions in the two wire chambers downstream of the  
<sub>157</sub> magnets to form a trajectory after the bend. We use the angles in the XZ plane  
<sub>158</sub> between the upstream and downstream trajectories to calculate the  $Z$  component of  
<sub>159</sub> the momentum as follows:

$$P_z = \frac{B_{eff}L_{eff}}{3.3(\sin(\theta_{DS}) - \sin(\theta_{US}))}, \quad (1)$$

<sub>160</sub> where  $B_{eff}$  is the effective maximum field in a square field approximation,  $L_{eff}$   
<sub>161</sub> is the effective length of both magnets (twice the effective length of one magnet),  
<sub>162</sub>  $\theta_{US}$  is the angle off the  $z$  axis of the upstream trajectory,  $\theta_{DS}$  is the angle off the  
<sub>163</sub>  $z$  axis of the downstream trajectory and  $3.3 c^{-1}$  is the conversion factor from [T·m]  
<sub>164</sub> to [MeV/c]. By using the hit positions on the third and fourth wire chamber, we  
<sub>165</sub> estimate the azimuthal and polar angles of the particle trajectory, and we are able to  
<sub>166</sub> calculate the other components of the momentum.

<sub>167</sub> The presence of multiple hits in a single wire chamber or the absence of hits in one  
<sub>168</sub> (or more) wire chambers can complicate this simple scenario. The first complication  
<sub>169</sub> is due to beam pile up, while the latter is due to wire chamber inefficiency. In the  
<sub>170</sub> case of multiple hits on a single WC, at most one wire chamber track is reconstructed  
<sub>171</sub> per event. Since the magnets bend particles only in the X direction, we assume  
<sub>172</sub> the particle trajectory to be roughly constant in the YZ plane, thus we keep the

173 combination of hits which fit best with a straight line. It is still possible to reconstruct  
174 the particle’s momentum even if the information is missing in either of the two middle  
175 wire chambers (WC2 or WC3), by constraining the particle trajectory to cross the  
176 plane in between the magnets.

177 Events satisfying the simplest scenario of one single hit in each of the four wire  
178 chambers form the “Picky Track” sample. We construct another, higher statistics  
179 sample, where we loosen the requirements on single hit and wire chamber efficiency:  
180 the “High Yield” sample. For LArIAT Run II, the High Yield sample is about three  
181 times the Picky Tracks statistics. For the first measurements of the LArIAT hadronic  
182 cross section, we use the Picky Tracks sample because the uncertainty on the momen-  
183 tum is smaller and the comparison with the beamline MC results is straightforward  
184 compared with the High Yield sample; a possible future update and cross check of  
185 these analysis would be the use of the High Yield sample.

186 **Four point track momentum uncertainty**

187 **0.2.3 Time-of-Flight System**

188 Two scintillator paddles, one upstream of the first set of WCs and one downstream  
189 of the second set of WCs form LArIAT time-of-flight (TOF) detector system.

190 The upstream paddle is made of a 10 x 6 x 1 cm scintillator piece, read out by  
191 two PMTs mounted on the beam left side which collect the light from light guides  
192 mounted on all four edges of the scintillator. The downstream paddle is a 14 x 14 x  
193 1 cm scintillator piece read out by two PMTs on the opposite ends of the scintillator,  
194 as shown in figure 5. The relatively thin width in the beamline direction minimizes  
195 energy loss of beam particles traveling through the scintillator material.

196 The CAEN 1751 digitizer is used to digitize the TOF PMTs signals at a sampling  
197 rate of 1 GHz. The 12 bit samples are stored in a circular memory buffer. At trigger  
198 time, data from the TOF PMTs are recorded to output in a 28.7  $\mu$ s windows starting

199 approximately 8.4  $\mu$ s before the trigger time.

200 **TOF functionality**

201 The TOF signals rise time (10-90%) is 4 ns and a full width, half-maximum of 9 ns  
202 consistent in time. The signal amplitudes from the upstream TOF and downstream  
203 TOF are slightly different: 200 mV for the upstream PMTs but only 50 mV for  
204 downstream PMTs. The time of the pulses was calculated utilizing an oversampled  
205 template derived from the data itself. We take the pulse pedestal from samples  
206 far from the pulse and subtract it from the pulse amplitude. We then vertically  
207 stretch a template to match the pedestal-subtracted pulse amplitude and we move  
208 it horizontally to find the time. With this technique, we find a pulse time-pickoff  
209 resolution better than 100 ps. The pulse pile up is not a significant problem given  
210 the TOF timing resolution and the rate of the particle beam. Leveraging on the  
211 pulses width uniformity of any given PMT, we flag events where two pulses overlap  
212 as closely in time as 4 ns with a 90% efficiency according to simulation.

213 We combine the pulses from the two PMTs on each paddle to determine the  
214 particles' arrival time by averaging the time measured from the single PMT, so to  
215 minimize errors due to optical path differences in the scintillator. However, a time  
216 spread of approximately 300 ps is present in both the upstream and downstream  
217 detectors, likely due to transit time jitter in the PMTs themselves.

218 **0.2.4 Punch-Through and Muon Range Stack Instruments**

219 The punch-through and the muon range stack (MuRS) detectors are located down-  
220 stream of the TPC. These detectors provide a sample of TPC crossing tracks without  
221 relying on TPC information and can be used to improve particle ID for muons and  
222 pions with momentum higher than 450 MeV/c.

223 The punch-through is simple sheet of scintillator material, read out by two PMTs.



Figure 5: Image of the down stream time of flight paddle, PMTs and relative support structure before mounting.

224 The MuRS is a segmented block of steel with four slots instrumented with scintillation  
225 bars. The four steel layers in front of each instrumented slot are 2 cm, 2 cm, 14 cm  
226 and 16 cm deep in the beam direction. Each instrumented slot is equipped with  
227 four scintillation bars each, positioned horizontally in the direction orthogonal to the  
228 beam. Each scintillator bar measures ? x ? x 2 cm and it is read out by one PMT.

229 The signals from both the punch-thorough and the MuRS PMTs are sent to a  
230 NIM discriminator. If the signal crosses the discriminator threshold, it is digitized in  
231 the CAEN V1740, same as the TPC. The sampling time of the CAEN V1740 is slow  
232 (of the order of 128 ns) and that the pulse shape information from the PMT is lost.  
233 A Punch-thorough and MuRS signal will then be simply a “hit” at a given time in  
234 the beamline event.

235 It is worth mentioning here the presence of an additional scintillation paddle  
236 between WC4 and the downstream paddle of the TOF system, called halo. The  
237 halo is a 39x38x1 cm<sup>3</sup> paddle with a 6.5 cm radius hole in the center, whose original  
238 function was to reject beam particles slightly offset from the beamline center. Data

239 from this paddle turned out to be unusable, so our data events include both particle  
240 going through the halo scintillation material or through the halo hole.

#### 241 0.2.5 LArIAT Cosmic Ray Paddle Detectors

242 LArIAT triggers both on beam events and on cosmic rays events. We perform this  
243 latter trigger by using two sets of cosmic ray paddle detectors (a.k.a. “cosmic towers”.)  
244 The cosmic towers frame the LArIAT cryostat, as one sits in the downstream left  
245 corner and the other sits in the upstream right corner of the cryostat. Two paddle  
246 sets of four scintillators pieces each make up each cosmic tower, an upper set and a  
247 lower set per tower. Of the four paddles, a couple of two matched paddles stands  
248 upright while the a second matched pair lies across the top of the assembly in the top  
249 sets (or across the bottom of the assembly in the bottom sets). The horizontal couple  
250 is used as a veto for particles traveling from inside the TPC out. The four signals  
251 from the vertical paddles along one of the body diagonals of the TPC are combined  
252 in a logical “AND”. This allows to select track due to cosmic muons at the ground  
253 level crossing the TPC along one of its diagonals. Cosmic ray muons whose average  
254 energy is in the few GeV range crossing both anode and cathode populate the events  
255 triggered this way. This particularly useful sample of tracks is associated can be used  
256 for many tasks; for example, we use anode-cathode piercing tracks to cross check  
257 the TPC electric field on data (see Appendix A), to calibrate the charge response of  
258 the TPC wires for the full TPC volume and to measure the electron lifetime in the  
259 chamber [16].

260 We retrieved the scintillation paddles from the decommissioning of the CDF de-  
261 tector at Fermilab and we used only the paddles with a counting efficiency greater  
262 than 95% and low noise at working voltage. The measured trigger rate of the whole  
263 system is 0.032 Hz, corresponding to  $\sim 2$  muons per minute.



Figure 6: Photograph of one of the scintillation counters used in the cosmic towers.

### 264 0.3 In the Cryostat

#### 265 0.3.1 Cryogenics and Argon Purity

266 LArIAT repurposed the ArgoNeuT cryostat [2] in order to use it in a beam of charged  
267 particles, and added a new process piping and a new liquid argon filtration system in  
268 FTBF. Inside the LArIAT experimental hall, the cryostat sits in the beam of charged  
269 particles with its horizontal main axis oriented parallel to the secondary beam,  $3^\circ$   
270 off axis from the tertiary beam

271 Two volumes make up LArIAT cryostat, shown in Figure 7: the inner vessel and  
272 the outer vessel. Purified liquid argon fills the inner vessel, while the outer volume  
273 provides insulation through a vacuum jacket equipped with layers of aluminized mylar  
274 superinsulation. The inner vessel is a cylinder of 130 cm length and 76.2 cm diameter,  
275 containing about 550 L of LAr, corresponding to a mass of 0.77 ton. We run the signal  
276 cables for the LArTPC and the high voltage feedthrough through a “chimney” at the  
277 top and mid-length of the cryostat.

278 Given the different scopes of the ArgoNeuT and LArIAT detectors, we made  
279 several modifications to the ArgoNeuT cryostat in order to use it in LArIAT. In  
280 particular, the modifications shown in Figure 8 were necessary to account for the  
281 beam of charged particles entering the TPC and to employ the new FTBF liquid

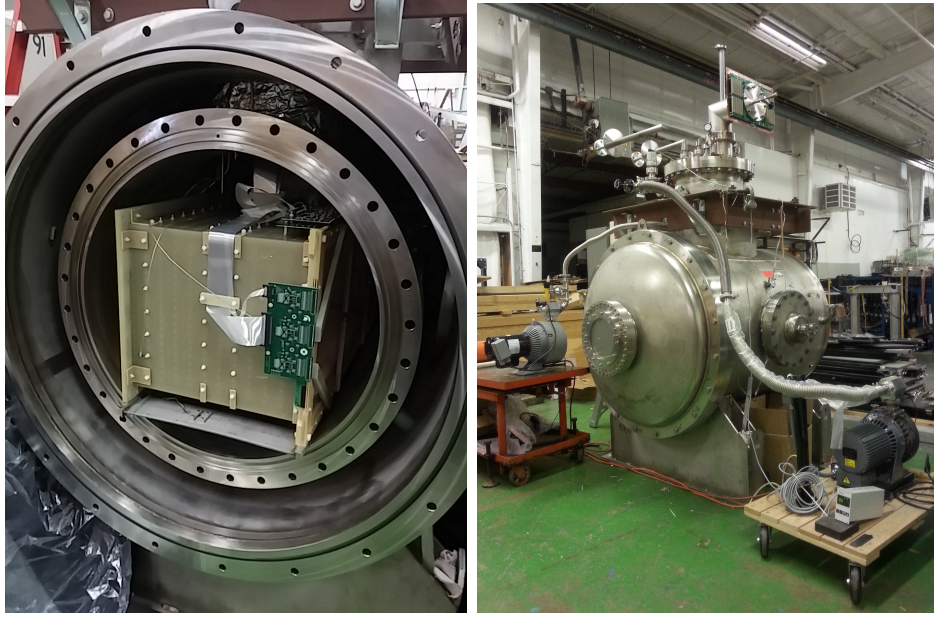


Figure 7: Left: the LArIAT TPC in the inner volume of the open cryostat. Right: cryostat fully sealed ready to be transported to FTBF.

282 argon purification system. We added a “beam window” on the front outer end cap  
 283 and an “excluder” on the inner endcap, with the purpose of minimizing the amount of  
 284 non-instrumented material upstream of the TPC’s active volume. The amount of non-  
 285 instrumented material in front of the TPC for LArIAT corresponds to  $\sim 0.3$  electron  
 286 radiation lengths ( $X_0$ ), to compare against the  $\sim 1.6X_0$  of ArgoNeuT. To allow studies  
 287 of the scintillation light, we added a side port feedthrough which enables the mounting  
 288 of the light collection system, as well as the connections for the corresponding signal  
 289 and high-voltage cables (see Section 0.3.3). We modified the bottom of the cryostat  
 290 adding Conflat and ISO flange sealing to connect the liquid argon transfer line to the  
 291 new argon cooling and purification system.

292 As in any other LArTPC, argon purity is a crucial parameter for LArIAT. Indeed,  
 293 the presence of contaminants affects both the basic working principles of a LArTPC,  
 294 as shown in section ???: electronegative contaminants such as oxygen and water de-  
 295 crease the number of ionization electrons collected on the wires after drifting through  
 296 the volume. In addition, contaminants such as Nitrogen decrease the light yield



Figure 8: Main modifications to the ArgoNeuT cryostat: 1) outlet for connection to the purification system at the bottom of the cryostat; 2) the “beam-window” on the outer endcap and “excluder” which reduces the amount of non-instrumented material before the TPC; 3) the side port to host the light collection system.

from scintillation light, especially in its slow component. In LArIAT, contaminations should not exceed the level of 0.2 parts per billion (ppb). We achieve this level of purity in several stages. The specifics required for the commercial argon bought for LArIAT are 2 parts per million (ppm) oxygen, 3.5 ppm water, and 10 ppm nitrogen. This argon is monitored with the use of commercial gas analyzer. Argon is stored in a dewar external to LArIAT hall and filtered before filling the TPC. LArIAT uses a filtration system designed for the Liquid Argon Purity Demonstrator (LAPD) [9]: half of a 77 liter filter contains a 4A molecular sieve (Sigma-Aldrich [17]) able to remove mainly water, while the other half contains BASF CU-0226 S, a highly dispersed copper oxide impregnated on a high surface area alumina, apt to remove mainly oxygen [4]. A single pass of argon in the filter is sufficient to achieve the necessary purity, unless the filter is saturated. In case the filter saturates, the media needs to be regenerated by using heated gas; this happened twice during the Run II period<sup>1</sup>. The

<sup>1</sup> We deemed the filter regeneration necessary every time the electron lifetime dropped under 100  $\mu$ s.

310 electron lifetime during the full LArIAT data taking are shown in Figure ???. The  
311 filtered argon reaches the inner vessel via a liquid feedthrough which is routed to the  
312 bottom of the cryostat. Argon is not recirculated in the system; rather, it boils off and  
313 vents to the atmosphere. During data taking, we replenish the argon in the cryostat  
314 every 6 hours to keep the TPC high voltage feedthrough and cold electronics always  
315 submerged. In fact, we constantly monitor the level, temperature, and pressure of  
316 the argon both in the commercial dewar and inside the cryostat during data taking.

### 317 **0.3.2 LArTPC: Charge Collection**

318 The LArIAT Liquid Argon Time Projection Chamber is a rectangular box of dimen-  
319 sions 47 cm (drift) x 40 cm (height) x 90 cm (length), containing 170 liters of Liquid  
320 Argon. The LArTPC three major subcomponents are

- 321 1) the cathode and field cage,
- 322 2) the wire planes,
- 323 3) the read-out electronics.

#### 324 **Cathode and field cage**

325 A G10 plain sheet with copper metallization on one of the 40 x 90 cm inner surfaces  
326 forms the cathode. A high-voltage feedthrough on the top of the LArIAT cryostat  
327 delivers the high voltage to the cathode; the purpose of the high voltage system  
328 (Figure 9) is to drift ionization electrons from the interaction of charged particles  
329 in the liquid argon to the wire planes. The power supply used in this system is a  
330 Glassman LX125N16 [13] capable of generating up to -125 kV and 16 mA of current,  
331 but operated at -23.5kV during LArIAT Run-II. The power supply is connected via  
332 high voltage cables to a series of filter pots before finally reaching the cathode.

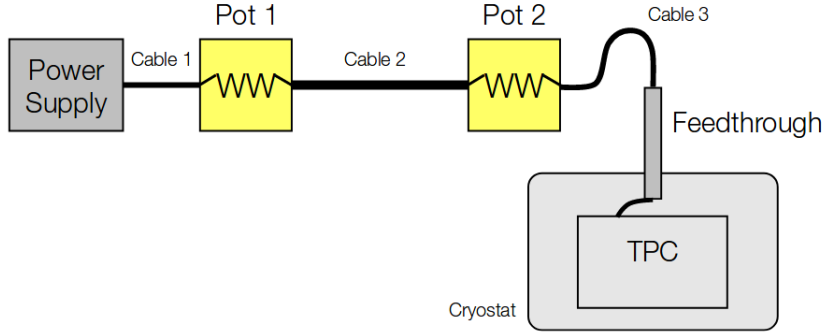


Figure 9: Schematic of the LArIAT high voltage system.

333        The field cage is made of twenty-three parallel copper rings framing the inner walls  
 334      of the G10 TPC structure. A network of voltage-dividing resistors connected to the  
 335      field cage rings steps down the high voltage from the cathode to form a uniform electric  
 336      field. The electric field over the entire TPC drift volume is 486 V/cm, as measured  
 337      in appendix A. The maximum drift length, i.e. the distance between cathode and  
 338      anode planes, is 47 cm.

339      **Wire planes**

340      LArIAT Run-II has three wire planes separated by 4 mm spaces: in order of increasing  
 341      distance from the cathode, they are the shield, the induction and the collection plane.  
 342      The “wire pitch”, i.e., the distance between two adjacent wires in a given plane, is  
 343      4 mm. The shield plane counts 225 parallel wires of equal length oriented vertically.  
 344      This plane is not connected with the read-out electronics; rather it shields the outer  
 345      planes from extremely long induction signals due to the ionization in the whole drift  
 346      volume. As the shield plane acts almost like a Faraday cage, the resulting shape of  
 347      signals in the first instrumented plane (induction) is easier to reconstruct. Both the  
 348      induction and collection planes count 240 parallel wires of different length oriented at  
 349       $60^\circ$  from the vertical with opposite signs. Electrons moving past the induction plane  
 350      will induce a bipolar pulse on its wires; the drifting electrons will be then collected

351 on the collection plane's wires, forming a unipolar pulse.

352 The three wire planes and the cathode form three drift volumes, as shown in Figure  
353 10. The main drift volume is defined as the region between the cathode plane and the  
354 shield plane (C-S). The other two drift regions are those between the shield plane and  
355 the induction plane (S-I), and between the induction plane and the collection plane  
356 (I-C). The electric field in these regions is chosen to satisfy the charge transparency  
357 condition and allow for 100% transmission of the drifting electrons through the shield  
358 and the induction planes.

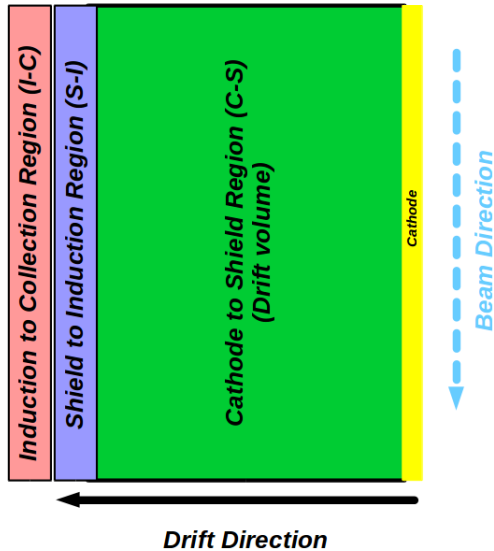


Figure 10: Schematic of the three drift regions inside the LArIAT TPC: the main drift volume between the cathode and the shield plane (C-S) in green, the region between the shield plane and the induction plane (S-I) in purple, and the region between the induction plane and the collection plane (I-C) in pink.

359 Table 1 provides the default voltages applied to the cathode and the shield, in-  
360 duction, and collection plane.

Table 1: Cathode and anode planes default voltages

Cathode	Shield	Induction	Collection
-23.17 kV	-298.8 V	-18.5 V	338.5 V

361 **Electronics**

362 Dedicated electronics read the induction and collection plane wires, for a total of  
363 480-channel analog signal path from the TPC wires to the signal digitizers. A digital  
364 control system for the TPC-mounted electronics, a power supply, and a distribution  
365 system complete the front-end system. Figure 11 shows a block diagram of the overall  
366 system. The direct readout of the ionization electrons in liquid argon forms typically  
367 small signals on the wires, which need amplification in oder to be processed. LArIAT  
368 performs the amplification stage directly in cold with amplifiers mounted on the TPC  
369 frame inside the liquid argon. The BNL ASICs adopted in LArIAT are designated as  
370 LArASIC, version 4-star and are the same used by the MicroBooNE experiment [10].  
371 The signal from the ASICs are driven to the other end of the readout chain, to the  
372 CAEN V1740 digitizers [6]. The CAEN V1740 has a 12 bit resolution and a maximum  
373 input range of 2 VDC, resulting in about 180 ADC count for a crossing MIP.

374 **0.3.3 LArTPC: Light Collection System**

375 The collection of scintillation photons is the second mechanism of particle detection  
376 in argon other than the ionization electrons. Over the course of LArIAT’s three years  
377 of data taking, the light collection system changed several times. We describe here  
378 the light collection system for Run II. Two PMTs, a 3-inch diameter Hamamatsu  
379 R-11065 and 2-inch diameter ETL D757KFL [1], as well as three SiPMs arrays (two  
380 Hamamatsu S11828-3344M 4x4 arrays and one single-channel SensL MicroFB-60035)  
381 are mounted on the PEEK support structure. PEEK screws into an access flange as  
382 shown in Figure 12, on the anode side, leaving approximately 5 cm of clearance from  
383 the collection plane.

384 Liquid argon scintillates in vacuum-ultraviolet (VUV) range at 128 nm; since  
385 cryogenic PMTs are not sensitive to VUV wavelengths, we need to shift the light to a  
386 range that is visible to the PMTs. In LArIAT, the wavelength shifting is achieved by

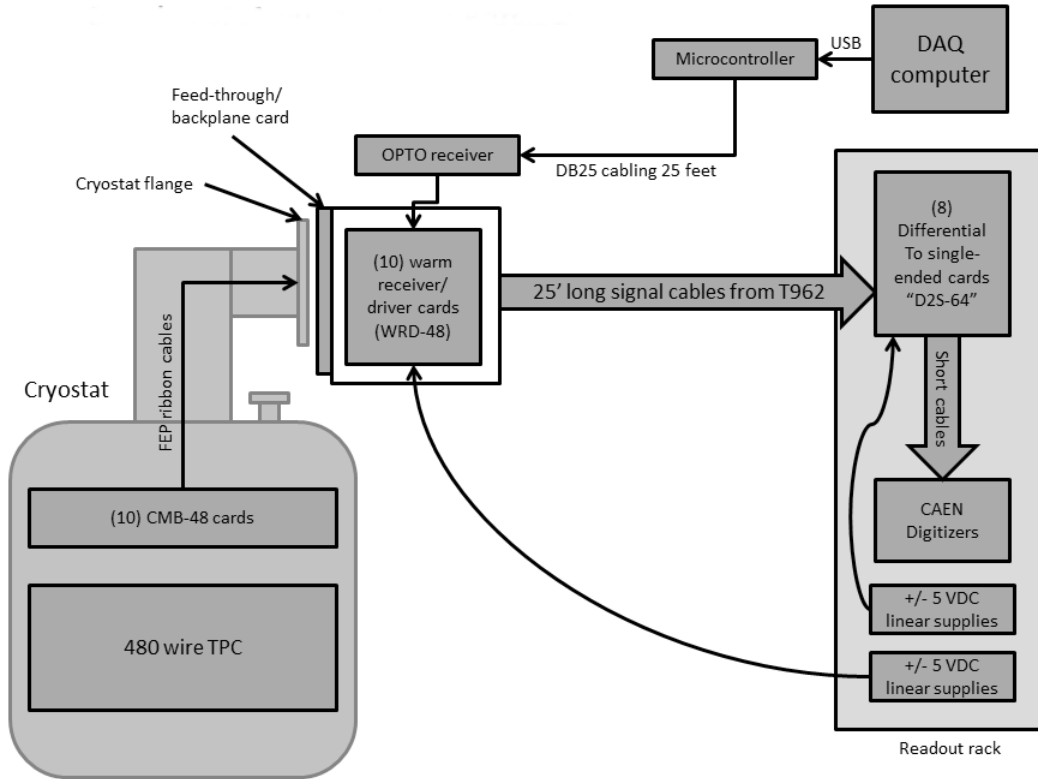


Figure 11: Overview of LArIAT Front End electronics.

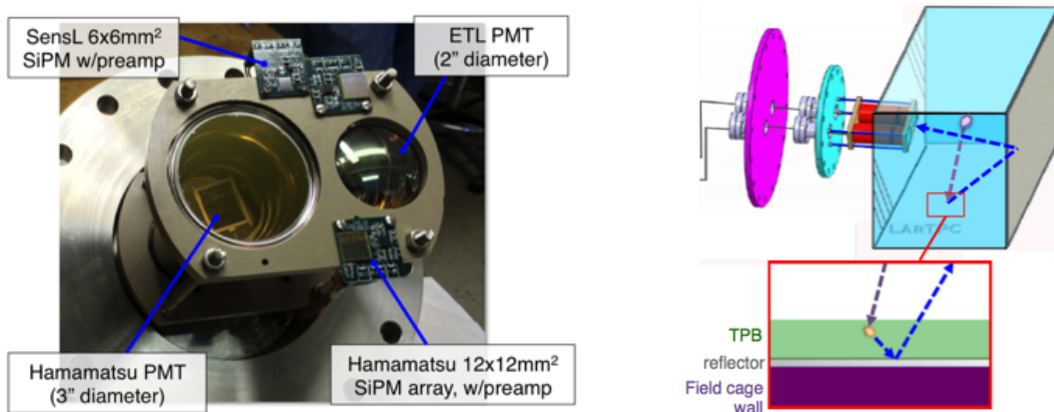


Figure 12: LArIAT's photodetector system for observing LAr scintillation light inside the TPC (left), and a simplified schematic of VUV light being wavelength-shifting along the TPB-coated reflecting foils (right).

387 installing highly-reflective 3M VIKUITI dielectric substrate foils coated with a thin  
388 layer of tetraphenyl-butadiene (TPB) on the four unbiased walls of the TPC. The  
389 scintillation light interaction with the TPB emits one or more visible photons, which  
390 are then reflected into the chamber. Thus, the light yield increases and results in  
391 higher uniformity of light across the TPC active volume, allowing the possibility of  
392 light-based calorimetry, currently under study.

393 For Run II, we coated the windows of the ETL PMT and the SensL SiPM with  
394 a thin layer of TPB. In doing so, some of the VUV scintillation light converts into  
395 visible right at the sensor faces, keeping information on the direction of the light  
396 source. Information about the light directionality is hindered for the light reflected  
397 on foils, as the reflection is uniform in angle.

## 398 0.4 Trigger and DAQ

399 The LArIAT DAQ and trigger system governs the read out of all the many subsystems  
400 forming LArIAT. The CAEN V1495 module [5] and its user-programmable FPGA are  
401 the core of this system. Every 10 ns, this module checks for matches between sixteen  
402 logical inputs and user-defined patterns in the trigger menu; if it finds a match for  
403 two consecutive clock ticks, that trigger fires.

404 LArIAT receives three logic signals from the Fermilab accelerator complex related  
405 to the beam timing which we use as input triggers: a pulse just before the beam, a  
406 pulse indicating beam-on, and a beam-off pulse.

407 The beam instruments, the cosmic ray taggers, and the light collection system  
408 provide the other NIM-standard logic pulse inputs to the trigger decision. We auto-  
409 matically log the trigger inputs configuration with the rest of the DAQ configuration  
410 at the beginning of each run.

411 Fundamental inputs to the trigger card come from the TOF (see section 0.2.3)

412 and the wire chambers (see section 0.2.2), as activity in these systems points to the  
413 presence of a charged particle in tertiary beam line. In particular, the discriminated  
414 pulses from the TOF PMTs form a NIM logic pulse for the trigger logic. We ask  
415 for a coincidence within a 20 ns window for all the pulses from the PMTs looking at  
416 the same scintillator block and use a delayed coincidence between the upstream and  
417 downstream paddle to inform the trigger decision. In order to form a coincidence  
418 between the upstream and downstream paddles, we delay the upstream paddle coin-  
419 cidence by 20 ns and widen it by 100 ns. The delay and widening are necessary to  
420 account for both lightspeed particles and slower particles (high-mass) to travel the  
421 6.5 m between the upstream and the downstream paddles. For the read out of the  
422 wire chambers, we use a total of sixteen multi-hit TDCs [14], four per chamber: two  
423 TDC per plane (horizontal and vertical), sixty-four wires per TDC. In each TDC, we  
424 keep the logical “OR” for any signal over threshold from the sixty-four wires. We  
425 then require a coincidence between the “OR” for the horizontal TDCs and the “OR”  
426 for the vertical TDCs: with this logic we make sure that at least one horizontal wire  
427 and one vertical wire saw significant signal in one wire chamber. The single logical  
428 pulse from each of the four wire chambers feeds into the first four inputs to the V1495  
429 trigger card. We require a coincidence within 20 ns of at least three logical inputs to  
430 form a trigger.

431 The cosmic towers (see Section 0.2.5) provide another primary input to the trigger,  
432 in order to capture long tracks from cosmic muons crossing the TPC. We use NIM  
433 modules to require coincidences between one upper and one lower paddle set of any  
434 opposite cosmic towers. The OR all the opposite towers’ coincidences is fed as an  
435 input to the trigger card.

436 We use the signal from the cryogenic PMTs (see Section 0.3.3) to form several  
437 interesting triggers. The coincidence of signals from all the PMT pulses within  $\sim$ 20 ns  
438 is an indication of ionizing radiation in the TPC and forms a trigger input. The

439 coincidence of two subsequent scintillation logic pulses delayed by a maximum of 7  $\mu$ s  
440 forms the Michel electron trigger.

## 441 0.5 Control Systems

442 LArIAT is a complex ensemble of systems which needed to be monitored simultaneously during data taking. We performed the monitoring of the systems operations with a slow control system, a DAQ monitoring system and a low level data quality monitoring described in the following sections.

### 446 Slow Control

447 We used the Synoptic Java Web Start framework [3] as a real-time display of subsystem conditions. Synoptic provides a Graphical User Interface that talks to the Fermilab Accelerator Control System via the ACNET protocol. Its simple GUI allowed us to change the operating parameters and to graph the trends of several variables of interest for all of the tertiary beam detectors. Among the most important quantities monitored by Synoptic there are the level of argon in both the inner vessel and the external dewar, the operating voltages of cathode and wire planes, of the PMTs and SiPMs, and of the four wire chambers, as well as the magnet temperatures. Figure 13 shows an example of the monitoring system. LArIAT uses the Accelerator Control NETwork system (ACNET) to monitor the beam conditions of the MCenter beamline. For example, the horizontal and vertical position of the beam at the first two wire chambers (WC1 and WC2) are shown in 14 as seen by the shifter during data taking.

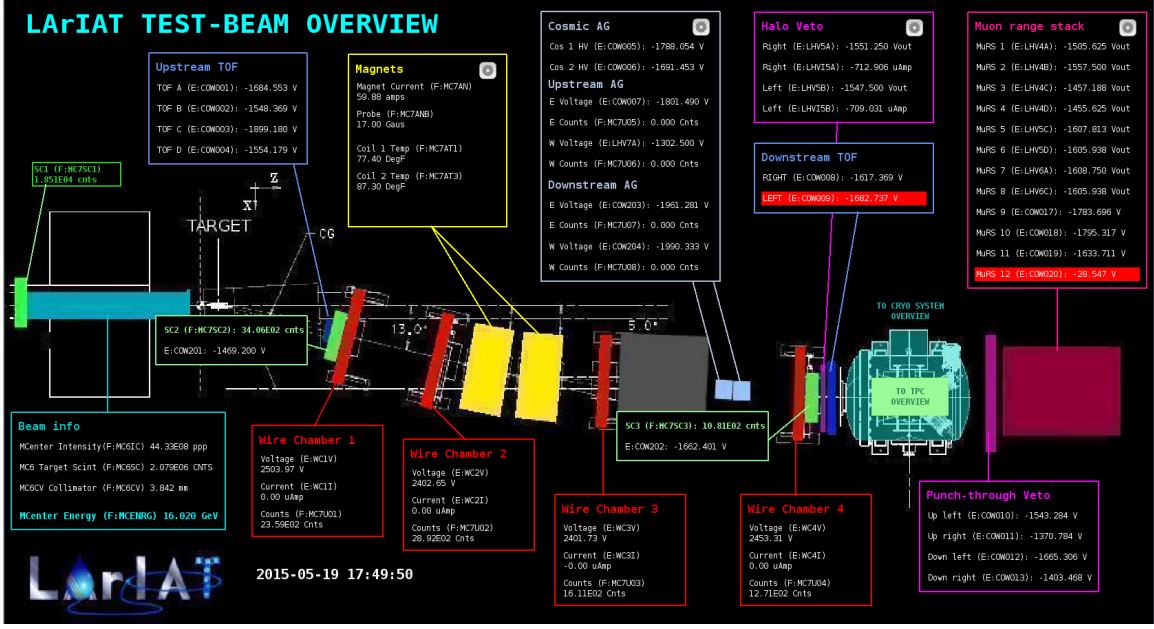


Figure 13: Interface of the Synoptic slow control system

## 460 DAQ Monitoring

461 We monitor the data taking and the run time evolution with the Run Status Webpage  
 462 (<http://lariat-wbm.fnal.gov/lariat/run.html>), a webpage updated in real-time. The  
 463 page displays, among other information, the total number of triggers in the event,  
 464 the total number of detectors triggered during a beam spill, the trigger patterns, the  
 465 number of times a particular trigger pattern was satisfied during a beam spill, and  
 466 the current time relative to the Fermilab accelerator complex supercycle. A screen  
 467 shot of the page is show in figure 15.

## 468 Data Quality Monitoring

469 We employ two systems to ensure the quality of our data during data taking: the  
 470 Near-Real-Time Data Quality Monitoring and the Event Viewer.

471 The Near-Real-Time Data Quality Monitoring (DQM) is a webpage which receives  
 472 updates from all the VME boards in the trigger system and displays the results of  
 473 a quick analysis of the DAQ stream of raw data on a spill-by-spill basis. The DQM

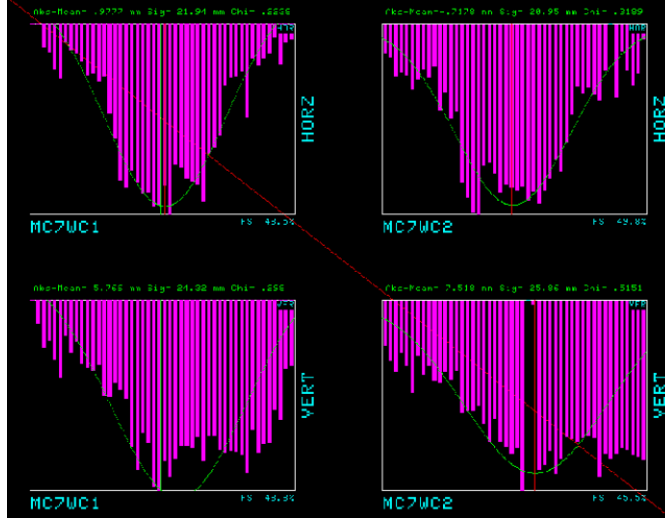


Figure 14: Beam position at the upstream wire chambers monitored with ACNET.

allows the shifter to monitor almost in real time (typically with a 2-minute delay) a series of low level-quantities and compare them to past collections of beam spills. Some of the variables monitored in the DQM are the pedestal mean and RMS on CAEN digitizer boards of the TPC wires and PMTs of the beamline detectors, the hit occupancy and timing plots on the wire chambers, and number of data fragments recorded that are used to build a TPC event. Abnormal values for low-level quantity in the data activates a series of alarms in the DQM; this quick feedback on the DAQ and beam conditions is fundamental to assure a fast debugging of the detector and a very efficient data taking during beam uptime.

The online Event Viewer displays a two dimensional representation (Wire vs Time) of LArIAT TPC events on both the Induction and the Collection planes in near real time. The raw pulses collected by the DAQ on each wire are plotted as a function of drift time, resulting in an image of the TPC event easily readable by the shifter. This tool guarantees a particularly good check of the TPC operation which activate an immediate feedback for troubleshooting a number of issues. For example, it is easy for the shifter to spot high occupancy events and request a reduction of the primary beam intensity, or to spot a decrease of the argon purity which requires the

<sup>491</sup> regeneration of filters, or to catch the presence of electronic noise and reboot the  
<sup>492</sup> ASICs. An example of high occupancy event is shown in 16.

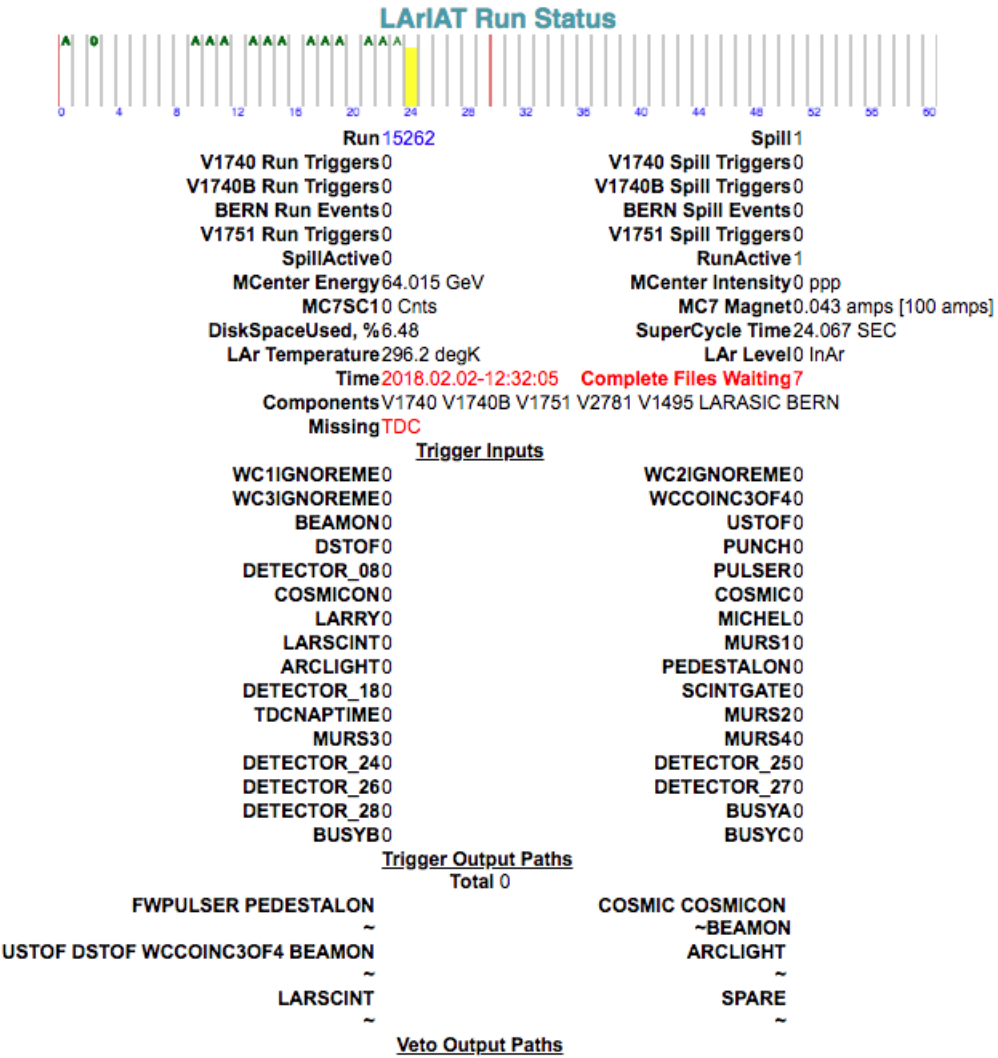


Figure 15: Run Status page at LArIAT downtime. At the top the yellow bar displays the current position in the Fermilab supercycle. Interesting information to be monitored by the shifter were the run number and number of spills, time elapsed from data taking (here in red), the energy of the secondary beam and the trigger paths.

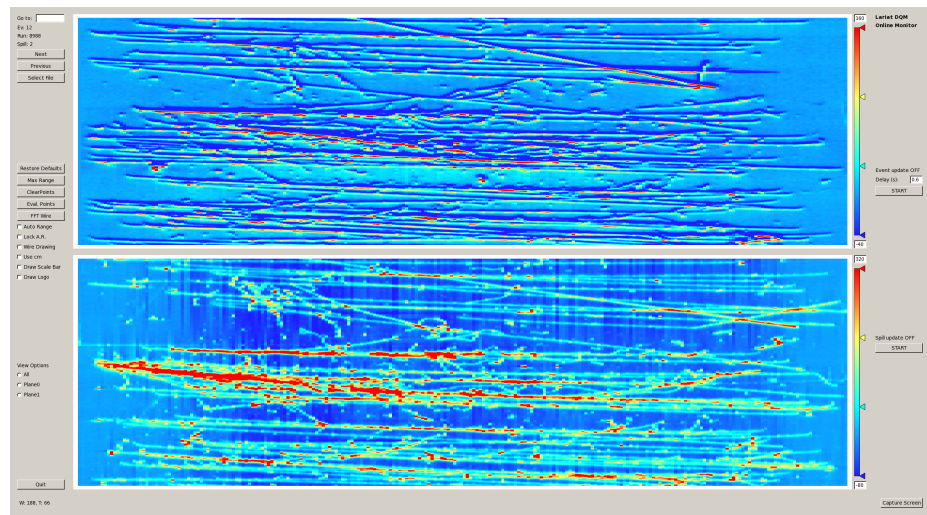


Figure 16: High occupancy event display: induction plane (top) and collection plane (bottom).

493 **Chapter 1**

494 **Total Hadronic Cross Section**

495 **Measurement Methodology**

496 section

497 **1.1 How to Measure a Hadron Cross Section in**  
498 **LArIAT**

499 We use both the LArIAT beamline detectors and the LArTPC information to measure  
500 the total hadronic cross sections in argon. Albeit with small differences, both the  $\pi^-$  -  
501 Ar and  $K^+$  - Ar total hadronic cross section measurements rely on the same procedure  
502 described in details in the following sections: we select the particle of interest using a  
503 combination of beamline detectors and TPC information (section 1.1.1), we perform a  
504 handshake between the beamline information and the TPC tracking to assure we are  
505 selecting the right TPC track (section 1.1.2), and we apply the “thin slice” method  
506 to get to the final result (section 1.1.3). At the end of this chapter, we show a cross  
507 check of this method against MC truth information (section 1.1.4).

508    **1.1.1 Event Selection**

509    **Beamline events**

510    As will be clear in section 1.1.3, beamline particle identification and momentum mea-  
511    surement before entering the TPC are fundamental information for the hadronic cross  
512    sections measurements in LArIAT. Thus, we apply selections to the LArIAT data to  
513    keep only events whose wire chamber and time of flight information is registered. Ad-  
514    ditionally, we perform a check of the plausibility of the trajectory inside the beamline  
515    detectors: given the position of the hits in the four wire chambers, we make sure the  
516    particle trajectory does not cross any impenetrable material such as the collimator  
517    and the magnets steel.

518    **Particle Identification in the beamline**

519    In data, the main tool to establish the identity of the hadron of interest is the LArIAT  
520    tertiary beamline, in its function of mass spectrometer. We combine the measurement  
521    of the time of flight,  $TOF$ , and the beamline momentum,  $p_{Beam}$ , to reconstruct the  
522    invariant mass of the particles in the beamline,  $m_{Beam}$ , as follows

$$m_{Beam} = \frac{p_{Beam}}{c} \sqrt{\left(\frac{TOF * c}{l}\right)^2 - 1}, \quad (1.1)$$

523    where  $c$  is the speed of light and  $l$  is the length of the particle trajectory between the  
524    time of flight paddles.

525    Figure 1.1 shows the mass distribution for the Run II negative polarity runs on  
526    the left and positive polarity runs on the right. We perform the classification of events  
527    into the different samples as follows:

528       •  $\pi, \mu, e$ :  $0 \text{ MeV} < \text{mass} < 350 \text{ MeV}$

529       • kaon:  $350 \text{ MeV} < \text{mass} < 650 \text{ MeV}$

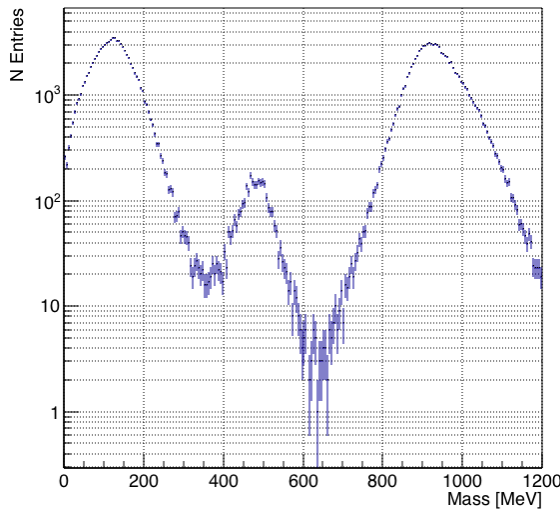


Figure 1.1: The mass plotted for a sample of Run-II events reconstructed in the beamline, negative polarity runs on the left and positive polarity runs on the right. The classification of the events into  $\pi$ ,  $\mu$ ,  $e$ , kaon, or proton is based on this distribution.[CHANGE PLOTS](#)

- 530     • proton:  $650 \text{ MeV} < \text{mass} < 3000 \text{ MeV}$ .

531     **Additional Particle Identification technique**

532     In the case of the  $\pi^-$ -Ar cross section, the resolution of beamline mass spectrometer is  
 533     not sufficient to select a beam of pure pions. In fact, muons and electrons survive the  
 534     selection on the beamline mass value. It is important to notice that the composition  
 535     of the negative polarity beam is mostly pions, as discussed in section ???. Anyhow,  
 536     we devise a selection on the TPC information to mitigate the presence of electrons  
 537     in the sample used for the pion cross section. The selection relies on the different  
 538     topologies of a pion and an electron event in the argon: while the former will trace  
 539     a track inside the TPC active volume, the latter will tend to “shower”, i.e. interact  
 540     with the medium, produce bremsstrahlung photons which pair convert into several  
 541     short tracks.

542 **Pile up mitigation**

543 The secondary beam impinging on LArIAT secondary target produces a plethora  
544 of particles. The presence of upstream and downstream collimators greatly abates  
545 the number of particles tracing down the LArIAT beamline. However, more than one  
546 beamline particles, or particles produced from the beam interaction with the beamline  
547 detectors, may sneak into the LArTPC during its readout time. The TPC readout  
548 is triggered by the actual particle firing the beamline detectors; we call “pile up”  
549 the additional traces in the TPC. We adjusted the primary beam intensity between  
550 LArIAT Run I and Run II to minimize the presence of events with high pile up  
551 particles in the data sample. For the cross section analyses, we remove events with  
552 more than 4 tracks in the first 14 cm upstream portion of the TPC from the sample.

553 **1.1.2 Wire Chamber to TPC Match**

554 For each event passing the selection on its beamline information we need to identify  
555 the track inside the TPC corresponding to the particle which triggered the beamline  
556 detectors, a procedure we refer to as “WC to TPC match” (WC2TPC for short).  
557 In general, the TPC tracking algorithm will reconstruct more than one track in the  
558 event, partially due to the fact that hadrons interact in the chamber and partially  
559 because of pile up particles during the triggered TPC drift time, as shown in figure  
560

560 **1.2. ADD EVENT DISPLAYS**

561 We attempt to uniquely match one wire chamber track to one and only one re-  
562 constructed TPC track. In data, this match leverages on a geometrical selection  
563 exploiting both the position of the wire chamber and TPC tracks, and the angle  
564 between them. We consider only TPC tracks whose first point is in the first 2 cm up-  
565 stream portion of the TPC for the match. We project the wire chamber track to the  
566 TPC front face where we define the  $x_{FF}$  and  $y_{FF}$  coordinates used for evaluating the  
567 match. We define  $\Delta X$  as the difference between the  $x$  position of the most upstream



Figure 1.2: Kaon candidate event: on the right, event display showing raw quantities; on the left, event display showing reconstructed tracks. In the reconstructed event display, different colors represent different track objects. A kink is visible in the kaon ionization, signature of a hadronic interaction: the tracking correctly stops at the kink position and two tracks are formed. An additional pile-up track is so present in the event (top track).

568 point of the TPC track and  $x_{FF}$ .  $\Delta Y$  is defined analogously. We define the radius  
 569 difference,  $\Delta R$ , as  $\Delta R = \sqrt{\Delta X^2 + \Delta Y^2}$ . The angle between the incident WC track  
 570 and the TPC track in the plane that contains them defines  $\alpha$ . If  $\Delta R < 4$  cm,  $\alpha < 8^\circ$ ,  
 571 a match between WC-track and TPC reconstructed track is found. We describe how  
 572 we determinate the best value for the radius and angular selection in sec ???. In MC,  
 573 we mimic the matching between the WC and the TPC track by constructing a fake  
 574 WC track using truth information at wire chamber four. We then apply the same WC  
 575 to TPC matching algorithm as in data. We discard events with multiple WC2TPC  
 576 matches. We use only those TPC tracks that are matched to WC tracks in the cross  
 577 section calculation.

578 **1.1.3 The Thin Slice Method**

579 **Cross Sections on Thin Target**

580 Cross section measurements on a thin target have been the bread and butter of  
581 nuclear and particle experimentalists since the Geiger-Marsden experiments [12]. At  
582 their core, these types of experiments consist in shooting a beam of particles with a  
583 known flux on a thin target and recording the outgoing flux.

584 In general, the target is not a single particle, but rather a slab of material con-  
585 taining many diffusion centers. The so-called “thin target” approximation assumes  
586 that the target centers are uniformly distributed in the material and that the target is  
587 thin compared to the interaction length so that no center of interaction sits in front of  
588 another. In this approximation, the ratio between the number of particles interacting  
589 in the target  $N_{Interacting}$  and number of incident particles  $N_{Incident}$  determines the  
590 interaction probability  $P_{Interacting}$ , which is the complementary to one of the survival  
591 probability  $P_{Survival}$ . Equation 1.2

$$P_{Survival} = 1 - P_{Interacting} = 1 - \frac{N_{Interacting}}{N_{Incident}} = e^{-\sigma_{TOT} n \delta X} \quad (1.2)$$

592 describes the probability for a particle to survive the thin target. This formula relates  
593 the total cross section  $\sigma_{TOT}$ , the density of the target centers  $n$  and the thickness of  
594 the target along the incident hadron direction  $\delta X$ , to the interaction probability<sup>1</sup>.  
595 If the target is thin compared to the interaction length of the process considered,  
596 we can Taylor expand the exponential function in equation 1.2 and find a simple  
597 proportionality relationship between the number of incident and interacting particles,

---

1. The scattering center density in the target,  $n$ , relates to the argon density  $\rho$ , the Avogadro number  $N_A$  and the argon molar mass  $m_A$  as  $n = \frac{\rho N_A}{m_A}$ .

598 and the cross section, as shown in equation 1.3:

$$1 - \frac{N_{\text{Interacting}}}{N_{\text{Incident}}} = 1 - \sigma_{\text{TOT}} n \delta X + O(\delta X^2). \quad (1.3)$$

599 Solving for the cross section, we find:

$$\sigma_{\text{TOT}} = \frac{1}{n \delta X} \frac{N_{\text{Interacting}}}{N_{\text{Incident}}}. \quad (1.4)$$

600 **Not-so-Thin Target: Slicing the Argon**

601 The LArIAT TPC, with its 90 cm of length, is not a thin target. However, the fine-  
602 grained tracking of the LArIAT LArTPC allows us to treat the argon volume as a  
603 sequence of many adjacent thin targets.

604 As described in Chapter 0, LArIAT wire planes consist of 240 wires each. The  
605 wires are oriented at +/- 60° from the vertical direction at 4 mm spacing, while the  
606 beam direction is oriented 3 degrees off the  $z$  axis in the  $XZ$  plane. The wires collect  
607 signals proportional to the energy loss of the hadron along its path in a  $\delta X = 4$   
608 mm/ $\sin(60^\circ) \approx 4.7$  mm slab of liquid argon. Thus, one can think to slice the TPC  
609 into many thin targets of  $\delta X = 4.7$  mm thickness along the direction of the incident  
610 particle, making a measurement at each wire along the path.

611 Considering each slice  $j$  a “thin target”, we can apply the cross section calculation  
612 from Eq. 1.4 iteratively, evaluating the kinetic energy of the hadron as it enters each  
613 slice,  $E_j^{\text{kin}}$ . For each WC-to-TPC matched particle, the energy of the hadron entering  
614 the TPC is known thanks to the momentum and mass determination by the tertiary  
615 beamline,

$$E_{\text{FrontFace}}^{\text{kin}} = \sqrt{p_{\text{Beam}}^2 - m_{\text{Beam}}^2} - m_{\text{Beam}} - E_{\text{loss}}, \quad (1.5)$$

616 where  $E_{\text{loss}}$  is a correction for the energy loss in the dead material between the

beamline and the TPC front face. The energy of the hadron at each slab is determined by subtracting the energy released by the particle in the previous slabs. For example, at the  $j^{th}$  point of a track, the kinetic energy will be

$$E_j^{kin} = E_{FrontFace}^{kin} - \sum_{i < j} \Delta E_i, \quad (1.6)$$

where  $\Delta E_i$  is the energy deposited at each argon slice before the  $j^{th}$  point as measured by the calorimetry associated with the tracking.

If the particle enters a slice, it contributes to  $N_{Incident}(E^{kin})$  in the energy bin corresponding to its kinetic energy in that slice. If it interacts in the slice, it then also contributes to  $N_{Interacting}(E^{kin})$  in the appropriate energy bin. The cross section as a function of kinetic energy,  $\sigma_{TOT}(E^{kin})$  will then be proportional to the ratio  $\frac{N_{Interacting}(E^{kin})}{N_{Incident}(E^{kin})}$ .

The statistical uncertainty for each energy bin is calculated by error propagation from the statistical uncertainty on  $N_{Incident}$  and  $N_{Interacting}$ . Since the number of incident hadrons in each energy bin is given by a simple counting, we assume that  $N_{Incident}$  is distributed as a poissonian with mean and  $\sigma^2$  equal to  $N_{Incident}$  in each bin. On the other hand,  $N_{Interacting}$  follows a binomial distribution: a particle in a given energy bin might or might not interact. The square of the variance for the binomial is given by

$$\sigma^2 = \mathcal{N} P_{Interacting} (1 - P_{Interacting}); \quad (1.7)$$

since the interaction probability  $P_{Interacting}$  is  $\frac{N_{Interacting}}{N_{Incident}}$  and the number of tries  $\mathcal{N}$  is  $N_{Incident}$ , equation 1.7 translates into

$$\sigma^2 = N_{Incident} \frac{N_{Interacting}}{N_{Incident}} \left(1 - \frac{N_{Interacting}}{N_{Incident}}\right) = N_{Interacting} \left(1 - \frac{N_{Interacting}}{N_{Incident}}\right). \quad (1.8)$$

$N_{Incident}$  and  $N_{Interacting}$  are not independent. The uncertainty on the cross section

637 is thus calculated as

$$\delta\sigma_{tot}(E) = \sigma_{tot}(E) \left( \frac{\delta N_{Interacting}}{N_{Interacting}} + \frac{\delta N_{Incident}}{N_{Incident}} \right) \quad (1.9)$$

638 where:

$$\delta N_{Incident} = \sqrt{N_{Incident}} \quad (1.10)$$

$$\delta N_{Interacting} = \sqrt{N_{Interacting} \left( 1 - \frac{N_{Interacting}}{N_{Incident}} \right)}. \quad (1.11)$$

### 639 1.1.4 Procedure testing with truth quantities

640 The  $\pi^-$ -Ar and  $K^+$ -Ar total hadronic cross section implemented in Geant4 can be  
641 used as a tool to validate the measurement methodology. We describe here a closure  
642 test done on Monte Carlo to prove that the methodology of slicing the TPC retrieves  
643 the underlying cross section distribution implemented in Geant4 within the statistical  
644 uncertainty.

645 For pions in the considered energy range, the Geant4 inelastic model adopted to  
646 is “BertiniCascade”, while the elastic model “hElasticLHEP”. For kaons, the Geant4  
647 inelastic model adopted to is “BertiniCascade”, while the elastic model “hElasti-  
648 cLHEP”.

649 For the validation test, we fire about 390000 pions and 140000 kaons inside the  
650 LArIAT TPC active volume using the Data Driven Monte Carlo (see section ??).  
651 We apply the thin-sliced method using only true quantities to calculate the hadron  
652 kinetic energy at each slab in order to decouple reconstruction effects from issues with  
653 the methodology. For each slab of 4.7 mm length along the path of the hadron, we  
654 integrate the true energy deposition as given by the Geant4 transportation model.  
655 Then, we recursively subtracted it from the hadron kinetic energy at the TPC front  
656 face to evaluate the kinetic energy at each slab until the true interaction point is

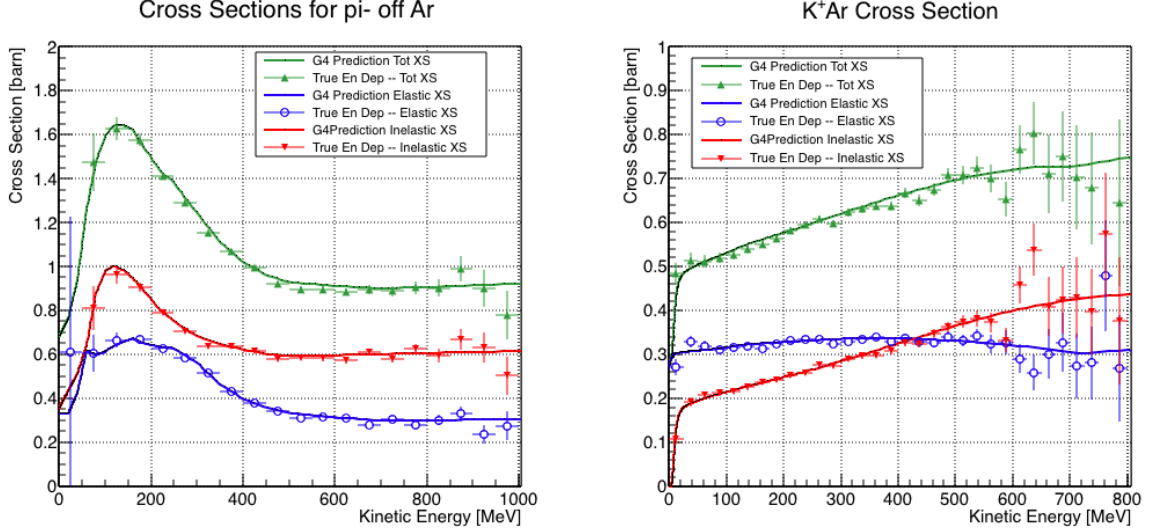


Figure 1.3: Hadronic cross sections for  $\pi^-$ -Ar (left) and  $K^+$ -Ar (right) implemented in Geant4 10.01.p3 (solid lines) overlaid the true MC cross section as obtained with the sliced TPC method (markers). The total cross section is shown in green, the elastic cross section in blue and the inelastic cross section in red.

reached. Doing so, we obtain the true interacting and incident distributions for the considered hadron and we obtain the true MC cross section as a function of the hadron true kinetic energy.

Figure 1.3 shows the total hadronic cross section for argon implemented in Geant4 10.01.p3 (solid lines) overlaid with the true MC cross section as obtained with the sliced TPC method (markers) for pions on the left and kaons on the right; the total cross section is shown in green, the elastic cross section in blue and the inelastic cross section in red. The nice agreement with the Geant4 distribution and the cross section obtained with the sliced TPC method gives us confidence in the validity of the methodology.

667 **Appendix A**

668 **Measurement of LArIAT Electric**  
669 **Field**

670 The electric field of a LArTPC in the drift volume is a fundamental quantity for  
671 the proper functionality of this technology, as it affects almost every reconstructed  
672 quantity such as the position of hits or their collected charge. Given its importance,  
673 we calculate the electric field for LArIAT with a single line diagram from our HV  
674 circuit and we cross check the obtained value with a measurement relying only on  
675 TPC data.

676 Before getting into the details of the measurement procedures, it is important to  
677 explicit the relationship between some quantities in play. The electric field and the  
678 drift velocity ( $v_{drift}$ ) are related as follows

$$v_{drift} = \mu(E_{field}, T)E_{field}, \quad (\text{A.1})$$

679 where  $\mu$  is the electron mobility, which depends on the electric field and on the  
680 temperature (T). The empirical formula for this dependency is described in [18] and  
681 shown in Figure A.1 for several argon temperatures.

682 The relationship between the drift time ( $t_{drift}$ ) and the drift velocity is trivially

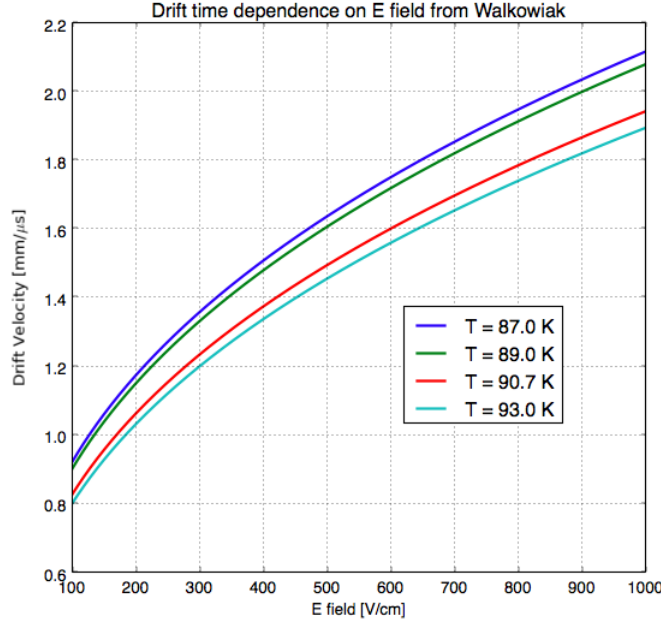


Figure A.1: Drift velocity dependence on electric field for several temperatures. The slope of the line at any one point represents the electron mobility for that given temperature and electric field.

Table A.1: Electric field and drift velocities in LArIAT smaller drift volumes

	Shield-Induction	Induction-Collection
$E_{filed}$	700.625 V/cm	892.5 V/cm
$v_{drift}$	1.73 mm/μs	1.90 mm/μs
$t_{drift}$	2.31 μs	2.11 μs

683 given by

$$t_{drift} = \Delta x / v_{drift}, \quad (\text{A.2})$$

684 where  $\Delta x$  is the distance between the edges of the drift region. Table A.1 reports the  
685 values of the electric field, drift velocity, and drift times for the smaller drift volumes.

686 With these basic parameters established, we can now move on to calculating the  
687 electric field in the main drift region (between the cathode and the shield plane).

## 688 Single line diagram method

689 The electric field strength in the LArIAT main drift volume can be determined know-  
 690 ing the voltage applied to the cathode, the voltage applied at the shield plane, and the  
 691 distance between them. We assume the distance between the cathode and the shield  
 692 plane to be 470 mm and any length contraction due to the liquid argon is negligibly  
 693 small ( $\sim 2$  mm).

694 The voltage applied to the cathode can be calculated using Ohm's law and the  
 695 single line diagram shown in Figure A.2. A set of two filter pots for emergency power  
 696 dissipation are positioned between the Glassman power supply and the cathode, one at  
 697 each end of the feeder cable, each with an internal resistance of  $40 \text{ M}\Omega$ . The output  
 698 current of the Glassman power supply is then used to determine the electric field  
 699 strength. Figure A.3 shows an average current of 0.004172 mA from the Glassman  
 700 power supply.

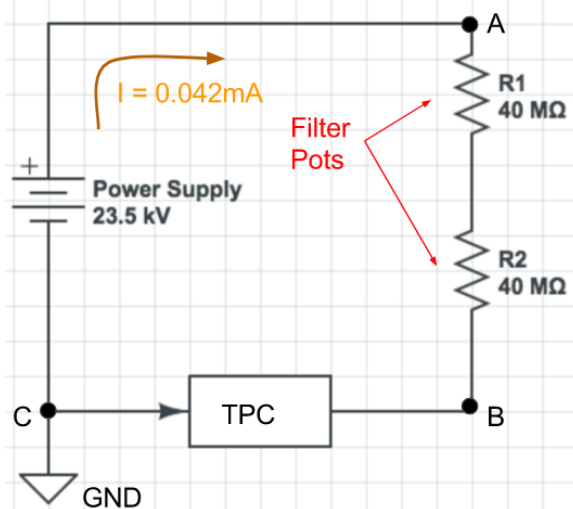


Figure A.2: get rid of current line LAr-IAT HV simple schematics.

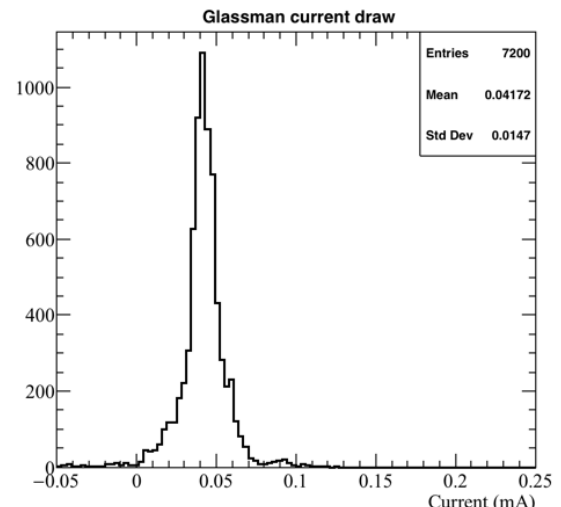


Figure A.3: **the axis is wrong!!** Current reading from the Glassman between May 25th and May 30th, 2016 (typical Run-II conditions).

701 Using this current, the voltage at the cathode is calculated as

$$V_{BC} = V_{PS} - (I \times R_{eq}) = -23.5 \text{ kV} + (0.00417 \text{ mA} \times 80 \text{ M}\Omega) = -23.17 \text{ kV}, \quad (\text{A.3})$$

702 where  $I$  is the current and  $R_{eq}$  is the equivalent resistor representing the two filter  
703 pots. The electric field, drift voltage, and drift time are then calculated to be

$$E_{\text{field}} = \frac{V_{BC} - V_{\text{shield}}}{\Delta x} = 486.54 \text{ V/cm} \quad (\text{A.4})$$

704 **E field using cathode-anode piercing tracks**

705 We devise an independent method to measure the drift time (and consequently drift  
706 velocity and electric field) using TPC cathode to anode piercing tracks. We use this  
707 method as a cross check to the single line method. The basic idea is simple:

- 708 0. Select cosmic ray events with only 1 reconstructed track
- 709 1. Reduce the events to the one containing tracks that cross both anode and  
710 cathode
- 711 2. Identify the first and last hit of the track
- 712 3. Measure the time difference between these two hits ( $\Delta t$ ).

713 This method works under the assumptions that the time it takes for a cosmic particle  
714 to cross the chamber ( $\sim \text{ns}$ ) is small compared to the charge drift time ( $\sim \text{hundreds}$   
715 of  $\mu\text{s}$ ).

716 We choose cosmic events to allow for a high number of anode to cathode piercing  
717 tracks (ACP tracks), rejecting beam events where the particles travel almost perpen-  
718 dicularly to drift direction. We select events with only one reconstructed track to  
719 maximize the chance of selecting a single crossing muon (no-michel electron). We  
720 utilize ACP tracks because their hits span the full drift length of the TPC, see figure

721 A.4, allowing us to define where the first and last hit of the tracks are located in space  
722 regardless of our assumption of the electric field.

723 One of the main features of this method is that it doesn't rely on the measurement  
724 of the trigger time. Since  $\Delta t$  is the time difference between the first and last hit of a  
725 track and we assume the charge started drifting at the same time for both hits, the  
726 measurement of the absolute beginning of drift time  $t_0$  is unnecessary. We boost the  
727 presence of ACP tracks in the cosmic sample by imposing the following requirements  
728 on tracks:

729 • vertical position (Y) of first and last hits within  $\pm 18$  cm from TPC center  
730 (avoid Top-Bottom tracks)

731 • horizontal position (Z) of first and last hits within 2 and 86 cm from TPC front  
732 face (avoid through going tracks)

733 • track length greater than 48 cm (more likely to be crossing)

734 • angle from the drift direction (phi in figure A.5) smaller than 50 deg (more  
735 reliable tracking)

736 • angle from the beam direction (theta in figure A.5) grater than 50 deg (more  
737 reliable tracking)

738 Tracks passing all these selection requirements are used for the  $\Delta t$  calculation.

739 For each track passing our selection, we loop through the associated hits in order  
740 to retrieve the timing information. The analysis is performed separately on hits on the  
741 collection plane and induction plane, but lead to consistent results. As an example  
742 of the time difference, figures A.6 and A.7 represent the difference in time between  
743 the last and first hit of the selected tracks for Run-II Positive Polarity sample on the  
744 collection and induction plane respectively. We fit with a Gaussian to the peak of the  
745  $\Delta t$  distributions to extract the mean drift time and the uncertainty associated with

746 it. The long tail at low  $\Delta t$  represent contamination of non-ACP tracks in the track  
 747 selection. We apply the same procedure to Run-I and Run-II, positive and negative  
 748 polarity alike.

749 To convert  $\Delta t$  recorded for the hits on the induction plane to the drift time we  
 750 utilize the formula

$$t_{drift} = \Delta t - t_{S-I} \quad (\text{A.5})$$

751 where  $t_{drift}$  is the time the charge takes to drift in the main volume between the  
 752 cathode and the shield plane and  $t_{S-I}$  is the time it takes for the charge to drift from  
 753 the shield plane to the induction plane. In Table A.1 we calculated the drift velocity  
 754 in the S-I region, thus we can calculate  $t_{S-I}$  as

$$t_{S-I} = \frac{l_{S-I}}{v_{S-I}} = \frac{4mm}{1.745mm/\mu s} \quad (\text{A.6})$$

755 where  $l_{S-I}$  is the distance between the shield and induction plane and  $v_{S-I}$  is the drift  
 756 velocity in the same region. A completely analogous procedure is followed for the hits  
 757 on the collection plane, taking into account the time the charge spent in drifting from  
 758 shield to induction as well as between the induction and collection plane. The value  
 759 for  $\Delta t_{drift}$ , the calculated drift velocity ( $v_{drift}$ ), and corresponding drift electric field  
 760 for the various run periods is given in Table A.2 and are consistent with the electric  
 761 field value calculated with the single line diagram method.

### Delta $t_{drift}$ , drift v and E field with ACP tracks

Data Period	$\Delta t_{Drift}$ [ $\mu s$ ]	Drift velocity [mm/ $\mu s$ ]	E field [V/cm]
RunI Positive Polarity Induction	$311.1 \pm 2.4$	$1.51 \pm 0.01$	$486.6 \pm 21$
RunI Positive Polarity Collection	$310.9 \pm 2.6$	$1.51 \pm 0.01$	$487.2 \pm 21$
RunII Positive Polarity Induction	$315.7 \pm 2.8$	$1.49 \pm 0.01$	$467.9 \pm 21$
RunII Positive Polarity Collection	$315.7 \pm 2.7$	$1.49 \pm 0.01$	$467.9 \pm 21$
RunII Negative Polarity Induction	$315.9 \pm 2.6$	$1.49 \pm 0.01$	$467.1 \pm 21$
RunII Negative Polarity Collection	$315.1 \pm 2.8$	$1.49 \pm 0.01$	$470.3 \pm 21$
Average Values	314.1	$1.50 \pm 0.01$	$474.3 \pm 21$

Table A.2:  $\Delta t$  for the different data samples used for the Anode-Cathode Piercing tracks study.

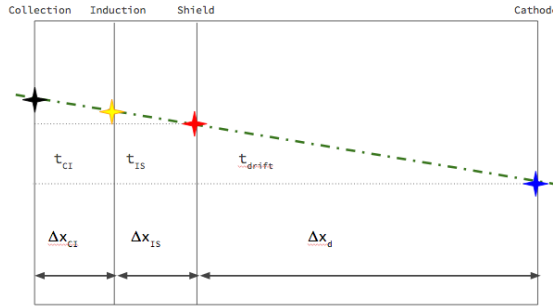


Figure A.4: Pictorial representation of the YX view of the TPC. The distance within the anode planes and between the shield plane and the cathode is purposely out of proportion to illustrate the time difference between hits on collection and induction. A ACP track is shown as an example.

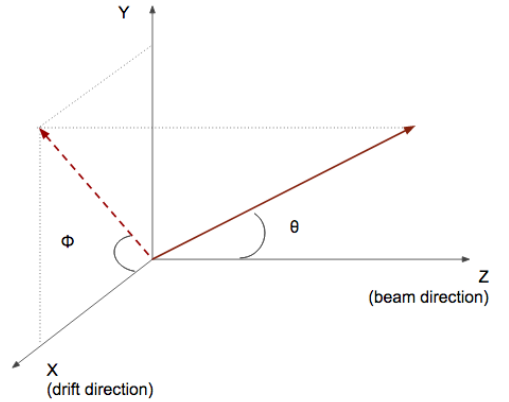


Figure A.5: Angle definition in the context of LArIAT coordinates system.

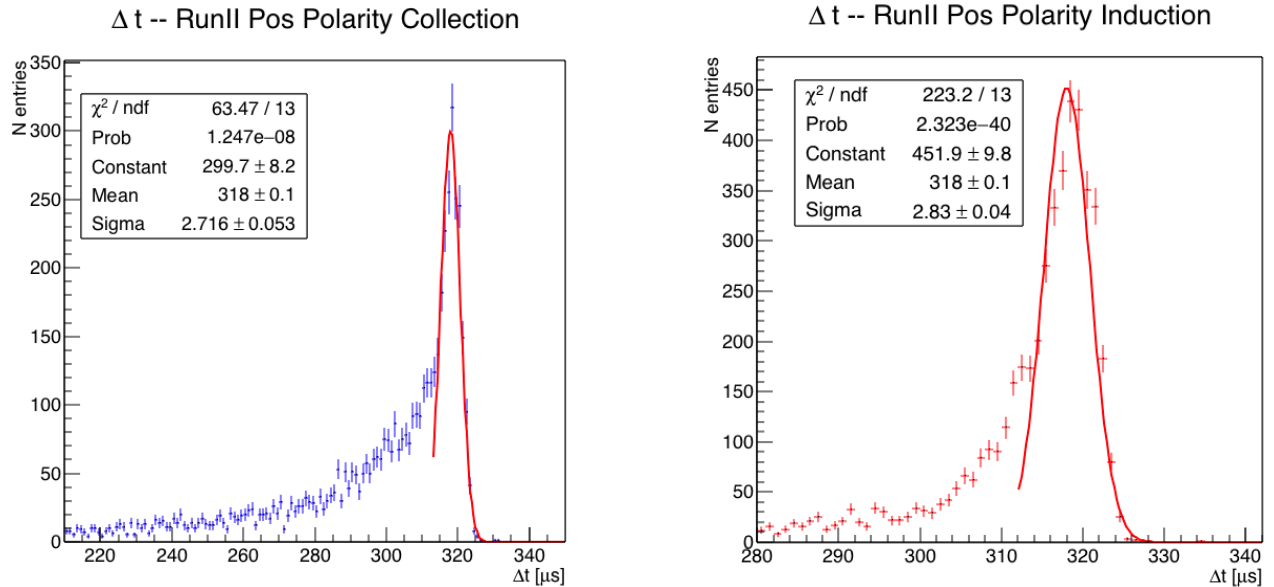


Figure A.6: Collection plane  $\Delta t$  fit for Run II positive polarity ACP data selected tracks.

Figure A.7: Induction plane  $\Delta t$  fit for Run II positive polarity ACP data selected tracks.

# <sup>762</sup> Bibliography

- <sup>763</sup> [1] R. Acciarri et al. Demonstration and Comparison of Operation of Photomultiplier Tubes at Liquid Argon Temperature. *JINST*, 7:P01016, 2012.
- <sup>764</sup>
- <sup>765</sup> [2] C. Anderson et al. The ArgoNeuT Detector in the NuMI Low-Energy beam line at Fermilab. *JINST*, 7:P10019, 2012.
- <sup>766</sup>
- <sup>767</sup> [3] Timofei Bolshakov Andrey Petrov. Java synoptic toolkit. Technical report, Sept 2010.
- <sup>768</sup>
- <sup>769</sup> [4] BASF Corp. 100 Park Avenue, Florham Park, NJ 07932 USA.
- <sup>770</sup>
- <sup>771</sup> [5] CAEN. Caen v1495 data sheet. Technical report, jan 2018.
- <sup>772</sup>
- <sup>773</sup> [6] CAEN. Caen v1740 data sheet. Technical report, jan 2018.
- <sup>774</sup>
- <sup>775</sup> [7] The LArIAT Collaboration. The liquid argon in a testbeam (lariat) experiment.
- <sup>776</sup>
- <sup>777</sup> [8] L. Aliaga et al. Minerva neutrino detector response measured with test beam data. *Nuclear Instruments and Methods in Physics Research Section A: Accelerators, Spectrometers, Detectors and Associated Equipment*, 789:28 – 42, 2015.
- <sup>778</sup>
- <sup>779</sup> [9] M Adamowski et al. The liquid argon purity demonstrator. *Journal of Instrumentation*, 9(07):P07005, 2014.

- 779 [10] R. Acciarri et al. Design and construction of the MicroBooNE detector. *Journal*  
780       *of Instrumentation*, 12(02):P02017–P02017, feb 2017.
- 781 [11] H Fenker. Standard beam pwc for fermilab. Technical report, Fermi National  
782       Accelerator Lab., Batavia, IL (USA), 1983.
- 783 [12] H. Geiger and E. Marsden. On a diffuse reflection of the formula-particles. *Pro-*  
784       *ceedings of the Royal Society A: Mathematical, Physical and Engineering Sci-*  
785       *ences*, 82(557):495–500, jul 1909.
- 786 [13] Glassman High Voltage, Inc., Precision Regulated High Voltage DC Power Sup-  
787       ply.
- 788 [14] S. Hansen, D. Jensen, G. Savage, E. Skup, and A. Soha. Fermilab test beam  
789       multi-wire proportional chamber tracking system upgrade. June 2014. Interna-  
790       tional Conference on Technology and Instrumentation in Particle Physics (TIPP  
791       2014).
- 792 [15] FM Newcomer, S Tedja, R Van Berg, J Van der Spiegel, and HH Williams.  
793       A fast, low power, amplifier-shaper-discriminator for high rate straw tracking  
794       systems. *IEEE Transactions on Nuclear Science*, 40(4):630–636, 1993.
- 795 [16] T. Yang R. Acciarri, M. Stancari. Determination of the electron lifetime in lariat.  
796       Technical report, March 2016.
- 797 [17] Sigma-Aldrich, P.O. Box 14508, St. Louis, MO 63178 USA.
- 798 [18] W. Walkowiak. Drift velocity of free electrons in liquid argon. *Nuclear Instru-*  
799       *ments and Methods in Physics Research Section A: Accelerators, Spectrometers,*  
800       *Detectors and Associated Equipment*, 449(1-2):288–294, jul 2000.